Posted on 24 Nov 2022 — The copyright holder is the author/funder. All rights reserved. No reuse without permission. — https://doi.org/10.1002/essoar.10509842.1 — This a preprint and has not been peer reviewed. Data may be preliminary.

Baroclinic control of Southern Ocean eddy upwelling near topography

Alice Barthel[1], Andrew McC. Hogg[2], Stephanie Waterman[3], and Shane Richard Keating[4]

[1]Los Alamos National Laboratory
[2]Australian National University
[3]University of British Columbia
[4]University of New South Wales

November 24, 2022

Abstract

In the Southern Ocean, mesoscale eddies contribute to the upwelling of deep waters along sloping isopycnals, helping to close the upper branch of the meridional overturning circulation. Eddy energy is not uniformly distributed along the Antarctic Circumpolar Current (ACC). Instead, 'hotspots' of eddy energy that are associated with enhanced eddy-induced upwelling exist downstream of topographic features. This study shows that, in idealized eddy-resolved simulations, a topographic feature in the ACC path can enhance and localize eddy-induced upwelling. However, the upwelling systematically occurs in regions where eddies grow through baroclinic instability, rather than in regions where eddy energy is large. Across a range of parameters, along-stream eddy growth rate is a more reliable indicator of eddy upwelling than traditional parameterizations such as eddy kinetic energy, eddy potential energy or isopycnal slope. Ocean eddy parameterizations should consider metrics specific to the growth of baroclinic instability to accurately model eddy upwelling near topography.

Baroclinic control of Southern Ocean eddy upwelling near topography

Alice Barthel[1], Andrew M. Hogg[2], Stephanie Waterman[3], and Shane Keating[4]

[1]Los Alamos National Laboratory, Los Alamos, NM, USA.
[2]Research School of Earth Sciences, Australian National University, Canberra, ACT, Australia.
[3]Department of Earth, Ocean and Atmospheric Sciences, University of British Columbia, Vancouver, BC, Canada.
[4]University of New South Wales, Sydney, NSW, Australia.

Key Points:

- Topography can support localised, enhanced cross-jet isopycnal transport driven by eddies.
- Transport occurs where baroclinic instability energizes eddies, not where eddy energy is high.
- In most cases, zonal growth of eddy energy is a more reliable indicator of cross-jet transport than metrics traditionally used.

Corresponding author: Alice Barthel, `ambarthel26@gmail.com`

Abstract

In the Southern Ocean, mesoscale eddies contribute to the upwelling of deep waters along sloping isopycnals, helping to close the upper branch of the meridional overturning circulation. Eddy energy is not uniformly distributed along the Antarctic Circumpolar Current (ACC). Instead, 'hotspots' of eddy energy that are associated with enhanced eddy-induced upwelling exist downstream of topographic features. This study shows that, in idealized eddy-resolved simulations, a topographic feature in the ACC path can enhance and localize eddy-induced upwelling. However, the upwelling systematically occurs in regions where eddies grow through baroclinic instability, rather than in regions where eddy energy is large. Across a range of parameters, along-stream eddy growth rate is a more reliable indicator of eddy upwelling than traditional parameterizations such as eddy kinetic energy, eddy potential energy or isopycnal slope. Ocean eddy parameterizations should consider metrics specific to the growth of baroclinic instability to accurately model eddy upwelling near topography.

Plain Language Summary

The Southern Ocean plays an essential role in redistributing heat, salt and biogeochemical tracers of importance in the climate system. In particular, locations in which strong ocean currents interact with large topographic features are hotspots for eddy-driven upward transport, and are crucial pathways to bring deep, carbon- and nutrient-rich waters to the surface. The processes which set the location and magnitude of this eddy 'upwelling' remain challenging to understand. This study uses a series of high-resolution idealized simulations in which an ocean jet encounters a piece of topography to investigate what controls the eddy upwelling near topography. We find that the upwelling due to eddies occurs in regions where the eddies are growing through a mechanism called 'baroclinic instability', rather than in regions where eddies are highly energetic or energized by other mechanisms. Regions of growing eddy energy are a simple, first-order indicator of regions of eddy upwelling, but future parameterisations of transport should consider the mechanism of instability to be more accurate.

1 Introduction

The Southern Ocean is an essential component of the global overturning circulation, which redistributes heat, salt and biogeochemical tracers of importance in the climate system (J. Marshall & Speer, 2012). In particular, sloping density surfaces (isopycnals) in the Southern Ocean provide an adiabatic route for deep waters to be upwelled to the surface. This along-isopycnal transport brings cold, carbon-rich waters to the surface (Le Quéré et al., 2007), imposing an important control on the Southern Ocean CO_2 sink and contributing to delayed warming of Southern Ocean waters (Armour et al., 2016).

Mesoscale eddies, which are particularly energetic in the Southern Ocean (Fu et al., 2010), play a dominant role in this along-isopycnal transport and therefore can have a critical influence on the associated mass, carbon and heat transports. Eddy activity in the Southern Ocean is not uniform in time or space. Zonal variations along the path of the Antarctic Circumpolar Current (ACC) are punctuated by regions of elevated eddy energy downstream of where the ACC interacts with major topographic features (Sokolov & Rintoul, 2009; Thompson, 2010; Frenger et al., 2015; Foppert et al., 2017), visible both at the surface (e.g. Fu et al., 2010) and at depth (e.g. Thompson & Naveira Garabato, 2014). These hotspots of eddy energy are favourable to stronger cross-jet exchange (Thompson & Sallée, 2012; Dufour et al., 2015) and enhanced upwelling of deep and intermediate waters (Viglione & Thompson, 2016; Tamsitt et al., 2017; Foppert et al., 2017).

Regions of elevated eddy energy are typically co-located with stationary meanders downstream of a topographic obstacle. The presence of these meanders, which are formed by arrested Rossby waves (Hughes & Ash, 2001), introduces non-zonal velocities, which lead to departures from the traditionally-assumed dynamical balances derived from a zonally-integrated view. The stationary meanders play an essential role in balancing zonal momentum and provide a mechanism for rapid barotropic adjustment of the flow to changes in forcing (Thompson & Naveira Garabato, 2014). These meanders appear to dominate the meridional heat transport (Dufour et al., 2012), but such heat transport predominantly occurs through transient eddies acting along the meander structure (Abernathey & Cessi, 2014). The essential role of transient eddies in this heat transport is visible when the transport is calculated in density-depth space (Zika et al., 2013) or following streamlines (Abernathey & Cessi, 2014).

The strength of eddy-induced transport in the Southern Ocean is often assumed to scale linearly with eddy kinetic energy (EKE) along the lines of the classical mixing length hypothesis (Prandtl, 1925; Holloway, 1986). For example, studies investigating the response of Southern Ocean circulation to changes in forcing often examine the response of EKE (e.g. Meredith & Hogg, 2006; Hogg et al., 2015; Patara et al., 2016), but few studies diagnose eddy-induced transport. Dufour et al. (2012) noted the increased southward transport due to transient and stationary eddies under increased wind forcing, but did not relate its response to that of EKE. However, there are no direct observations or modelling studies which support a direct, local proportionality between EKE and eddy-induced upwelling. On the contrary, Tamsitt et al. (2017) reports enhanced upwelling upstream of EKE maxima, but does not provide a dynamical explanation for this spatial separation. Likewise, Foppert et al. (2017) noted an offset between eddy heat fluxes and EKE in the Drake Passage, and suggest that the sea surface height deviation (a proxy for eddy potential energy, EPE) is a better indicator of the divergent eddy heat flux and, by extension, eddy upwelling owing to a direct connection to baroclinic instability (Watts et al., 2016). This offset is also found in the idealised simulations of Bischoff & Thompson (2014), which notes that EKE is not co-located with the steepest isopycnal slopes. An examination of how topography modulates eddy-induced upwelling and, further, an identification of the relationship between eddy energy and the mechanisms controlling upwelling location and magnitude are needed, in particular to inform our design of eddy upwelling proxies.

This study focuses on how a single unstable jet in a 2-layer system supports intense, localised, isopycnal upwelling associated with transient eddies. This jet is an analogue for a single filament of the ACC; the simplicity of this system allows unambiguous definition of cross-jet volume transport to quantify eddy upwelling, revealing insights that are not possible in a more comprehensive model. In particular, the question of whether local eddy energy (EE), or one of its constituents (EKE or EPE), is a good indicator of local eddy-induced upwelling is examined. Lastly, we show that a simple parameterisation of eddy-induced upwelling based on the zonal evolution of eddy energy provides a better representation of the zonal variability of upwelling around topography, compared with other proposed parameterisations based on EKE, EPE or time-mean isopycnal slope.

2 Methods

2.1 Model configuration

Our model simulations are designed to represent the interactions between a baroclinic ocean jet and an isolated topographic feature, in a configuration relevant to the

Southern Ocean (see Fig. 1). The set-up used is identical to that of Barthel et al. (2017). The model configuration is a channel on a β-plane, with dimensions of 9600 km $\times$ 1600 km and a horizontal resolution of 4 km. It consists of two isopycnal layers. We use MOM6 (Adcroft et al., 2019) to solve the hydrostatic thickness-weighted primitive equations under the Boussinesq approximation. The background horizontal viscosity is parameterised with a biharmonic horizontal viscosity of $A_4 = 1.5 \times 10^9$ m^4 s^{-1} to ensure numerical stability, while bottom friction is modelled by a weak quadratic bottom drag (with $C_{drag} = 5 \times 10^{-4}$). The dynamics in the interior of the channel are purely adiabatic.

The channel is forced to sustain an eastward-flowing jet (Fig. 1) by restoring the stratification at the western boundary. The jet characteristics are representative of a typical frontal jet observed in the Southern Ocean, with a 50-to-150-km-wide jet core containing peak velocities of 0.5-1 m s^{-1} (in the upper 1000 m), while velocity below 1000 m is of order 0.1 m s^{-1}(Waterman et al., 2013; Sheen et al., 2014). The eastern boundary also features a 'sponge' region where isopycnal heights are restored to allow the flow to readjust to the inflowing conditions. This boundary forcing of the flow provides a direct control of the jet structure at the inflow, as well as prescribing the total zonal transport. In this regard, this study differs from wind-driven channel studies which rely on a wind-friction equilibration (e.g. Bischoff & Thompson, 2014; Chapman et al., 2015) and can feature significantly different zonal transports depending on the presence of bottom topography (see Abernathey & Cessi, 2014, their Fig. 8). Stratification is also restored at the northern and southern boundaries, thus sustaining a large-scale meridional isopycnal slope, with the upper layer shoaling southward. This combination of forcing allows a non-zero residual overturning circulation to emerge in the domain, as it does in the Southern Ocean (e.g. G. J. Marshall, 2003; Lumpkin & Speer, 2007).

To explore topographic control of eddy-driven isopycnal upwelling, we compare flat-bottom simulations with cases which include either a circular seamount, or a meridional ridge, with a range of heights (0-500m). The range of topographic heights is small (compared with the Southern Ocean) because the topography has a disproportionately large effect in a two-layer system.

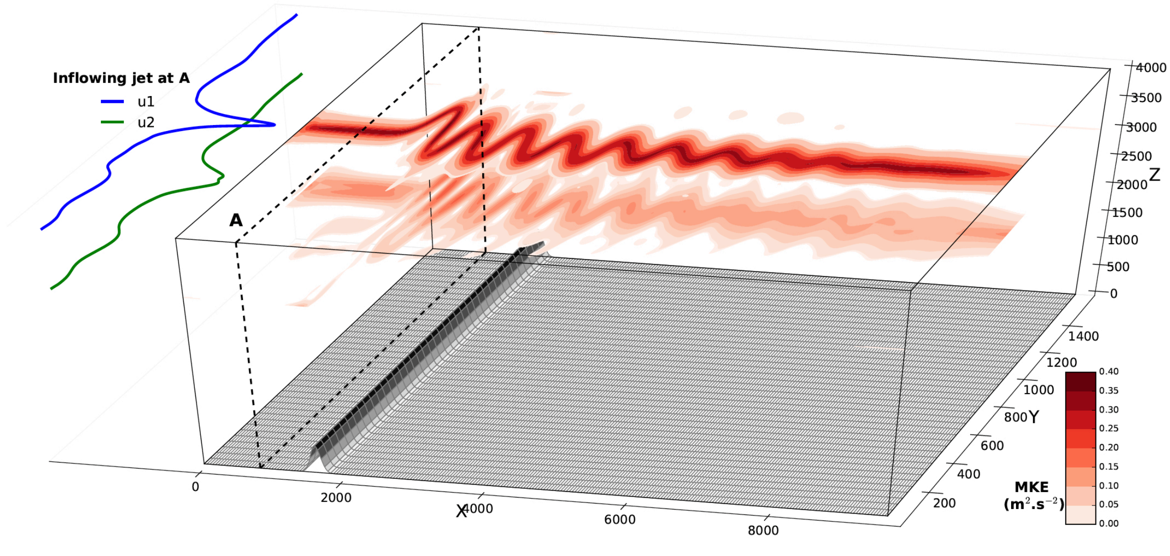

Figure 1. Model domain. A prescribed 2-layer jet flows eastward over topography, leading to stationary meanders downstream of topography. The maximum inflow velocities at section A are 0.7 $m.s^{-1}$ for the upper layer and 0.3 $m.s^{-1}$ for the lower layer.

2.2 Quantifying meridional transport

We diagnose the eddy-driven upwelling by quantifying the southward volume transport due to transient eddies in the upper, southward-shoaling isopycnal layer. Importantly, we account for the presence of stationary meanders downstream of topography by isolating the volume transport across the time-mean jet axis (hereafter the cross-jet transport). As our simulations have only one southward-shoaling layer, we sidestep the difficulties of defining a depth-dependent jet axis and focus on the transport by eddies across the contour of maximum upper-layer time-mean velocity. The transport, T, perpendicular to the time-mean velocity field is written as

$$T(x, y) = \overline{h_1 \mathbf{u}_1} \times \frac{\overline{\mathbf{u}_1}}{|\overline{\mathbf{u}_1}|} = \overline{h'_1 \mathbf{u'}_1} \times \frac{\overline{\mathbf{u}_1}}{|\overline{\mathbf{u}_1}|}, \quad (1)$$

where h_1 is the thickness and $\mathbf{u}_1$ is the horizontal velocity in the upper layer. The overbar indicates the time-mean of a quantity, and the prime is the deviation from that mean (i.e. the eddy component). By construction, only the eddy quantities contribute to the net transport across the time-mean velocity field. The cross-jet transport, X_{jt}, is defined on the jet axis:

$$X_{jt} = T(x, y_m(x)), \quad (2)$$

where y_m is the value of y for which $|\overline{\mathbf{u_1}}|$ is maximal. We count the transport as positive when it is southward, i.e. when it is associated with upwelling along the isopycnal layer.

The advantage of the above definition is that it allows us to robustly compare the net transport by eddies in the presence stationary meanders that form downstream of topographic obstacles. As stationary meanders have significant time-mean meridional velocities, they would have an alternating signal in southward and northward transport across a fixed latitude line (see Hallberg & Gnanadesikan, 2001, for a discussion on transport across streamlines versus fixed contours). Calculating the cross-jet transport at the jet axis allows a more meaningful comparison of net cross-jet transport between cases with and without jet meanders.

3 Results

3.1 Eddy-driven upwelling

The mean flow state from three selected runs is presented in Fig. 2. In each case the inflowing jet becomes unstable as it evolves eastward. The eddy energy (sum of EKE and EPE; indicated by colours in the upper panel of each subplot) has a distinct spatial pattern, growing with x as the flow evolves, with an along-stream maximum (highlighted by the red vertical bar in the lower panel). Eddy energy then remains constant or decays with further distance downstream. The qualitative evolution of eddy energy is similar in all three cases, although the zonal extent of the eddy energy growth region and the magnitude of the eddy energy depends on the nature of the topography. Similar results are obtained if we examine EKE and EPE individually (not shown).

The transient motions lead to an eddy-induced upwelling, quantified by the eddy-induced thickness transport across the time-mean jet axis (cyan arrows in Fig. 2). This transport also has zonal variations along the jet axis. In the case of the jet evolving over a flat bottom (Fig. 2a), the transport is southward, and preferentially takes place in a limited region (1500 km $< x <$ 3100 km). Further downstream, both southward and northward flux can occur locally, but these fluxes contribute little to the net transport. The bulk of the eddy-induced southward transport is localised in the region of eddy energy growth, with a 99% correlation between the zonal variations in the zonally integrated cumulative transport and local eddy energy (Fig. 2a, lower subpanel).

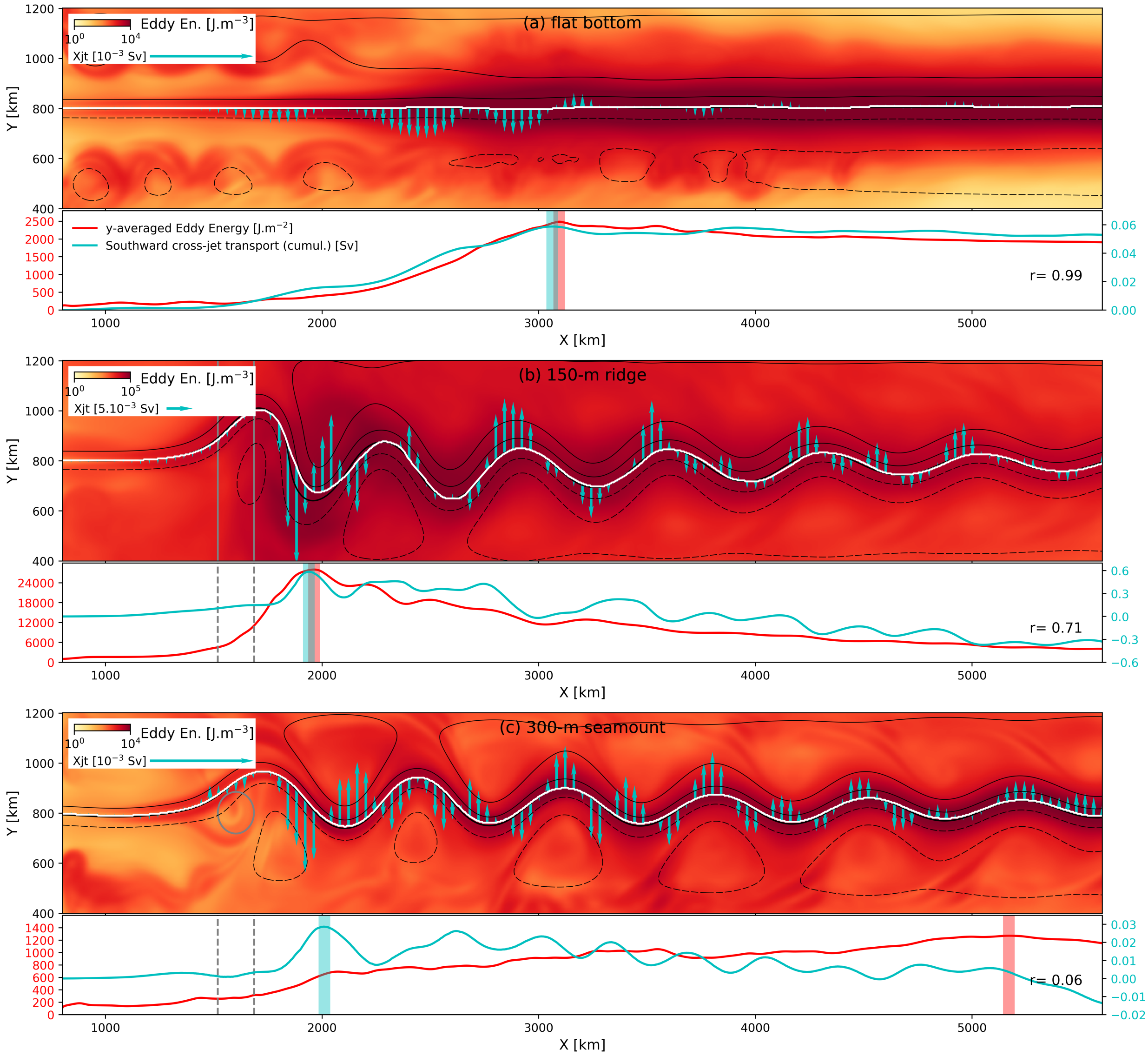

Figure 2. Eddy energy and cross-jet transport for a) flat bottom, b) 150m-tall ridge, c) 300m-tall seamount. In each subplot, the upper panel shows eddy energy (colours), the time-mean upper layer streamfunction (black contours), the time-mean jet axis (white line) and southward cross-jet volume transport (cyan arrows); the lower panel shows eddy energy integrated across the jet (red line, with the maximum value indicated by the vertical red bar) and the zonally integrated cumulative southward cross-jet transport (cyan line, with the maximum value indicated by the vertical cyan bar). Note that the 150 m ridge case (panel b) has significantly higher eddy energy and cross-jet transport, and thus has a different colour scale and arrow length scale.

In the presence of topography (illustrated by the 150 m ridge case; Fig. 2b), localised regions of enhanced eddy-induced cross-jet transport persist. The signature of the stationary meanders is visible in the eddy-induced cross-jet transport variability (manifested as alternating regions of southward and northward transport), making it difficult to distinguish the net effect of eddies. It is therefore especially helpful in this case to consider zonally integrated cumulative transport (cyan line, Fig. 2b, lower subpanel). This metric shows that the region immediately downstream of the ridge ($x = 1500 - 2000$ km) contributes significantly to the net southward transport relative to the regions further downstream. Around $x \approx 2000$ km (highlighted by the cyan vertical bar), there is a transition between a region of net southward transport ($x < 2000$ km) and a region of net northward transport ($x > 2000$ km). In some cases, the cumulative transport at $x = 6000$ km is northward, which may be due to the lack of disturbances to break down the meanders downstream. The close relationship between zonal growth of eddy energy and southward cross-jet transport, seen in the flat bottom case, also holds in the 150m ridge case (71% correlation).

Most of the simulations with topography conducted in this study provided results that are qualitatively similar to the 150m ridge case (not shown). However, the third case presented in Fig. 2, that with a 300 m high seamount, is one of the exceptions. This case is consistent with the results above in that it shows a qualitatively similar zonal evolution of eddy energy, and regions of preferential cross-jet transport immediately downstream of topography, but differs in the lack of correlation between along-stream eddy growth and cumulative southward transport. The break-down in this relationship provides insights into the underlying dynamics at play, and is explored in more detail in the next section.

In summary, two main points emerge from examination of the along-stream variations of eddy energy and transport in these idealised simulations. First, the presence of topography leads to enhanced eddy-induced cross-jet transport localised immediately downstream of the topographic obstacle, relative to the same jet evolving over a flat bottom. The magnitude and location of the eddy-induced transport depend on the properties of the topography present. Second, eddy energy and eddy-induced cross-jet transport ('eddy upwelling') have distinct zonal distributions. This transport tends to be localised in the region of along-stream eddy growth, but exceptions can occur where eddy-induced transport occurs in a region of smaller zonal extent than eddy energy growth.

3.2 Mechanism for topographic control

We probe the dynamics underpinning the differing spatial distributions of eddy energy and eddy-induced transport by looking at the two instability mechanisms that energise the eddy field in the 300 m seamount case (Fig. 3b), and comparing them with the flat-bottom case (Fig. 3a). Following the thickness-weighted energetics approach used in Aiki & Richards (2008) and Barthel et al. (2017), we diagnose the eddy-mean flow energy conversions due to 1) the work of interfacial form stress, $-\widehat{\mathbf{u}_1} \cdot \overline{h_1' \nabla \phi_1'}$ (where ϕ_1 is the Montgomery potential and $'$ denotes the anomaly from the $\overline{\cdot}$ time mean), responsible for the generation of eddy energy in baroclinic instability (dark blue lines), and 2) the work of Reynolds stress associated with horizontal convergence of momentum in the upper layer, associated with barotropic instability (black lines) $\rho_0 \widehat{\mathbf{u}_1} \cdot \nabla \cdot \overline{(h_1 \mathbf{u}_1'' \otimes \mathbf{u}_1'')}$, where $\widehat{\mathbf{u}_1}$ and $\mathbf{u}_1''$ are the thickness-weighted mean upper-layer velocity and the deviation from that mean, respectively. The outer product of two vectors is denoted by $\otimes$, and ρ_0 is the reference density of the Boussinesq approximation (see Barthel et al., 2017, for the full derivation).

The 300 m seamount is a helpful case to disentangle the contributions of form stress and Reynolds stress because they have distinct zonal patterns (Fig. 3b). These patterns indicate that the eddy-induced transport is associated exclusively with baroclinic instability (i.e. positive conversion of energy into the eddy field via form stress). This relationship is consistent with our conceptual understanding that baroclinic instability contributes to flattening isopycnals, and with observations in Drake Passage that indicate the eddy heat flux is best aligned with the production of EPE (Watts et al., 2016; Foppert et al., 2017). These results further suggest that the zonally-averaged link between interfacial form stress and meridional thickness flux (e.g. Olbers et al., 2004) may apply at the local scale. Understanding that the mechanism for eddy-induced transport is baroclinic instability acting as a source of eddy energy is consistent with the alignment of the region of eddy upwelling with the region of along-stream eddy growth, rather than with regions of elevated eddy energy.

The relationship between eddy upwelling and the action of eddy form stress in energising the eddy field is robust across all simulations, both with and without topography. In most cases, the region of southward eddy transport extends over the entire region of along-stream eddy growth because both energy conversion terms have the same

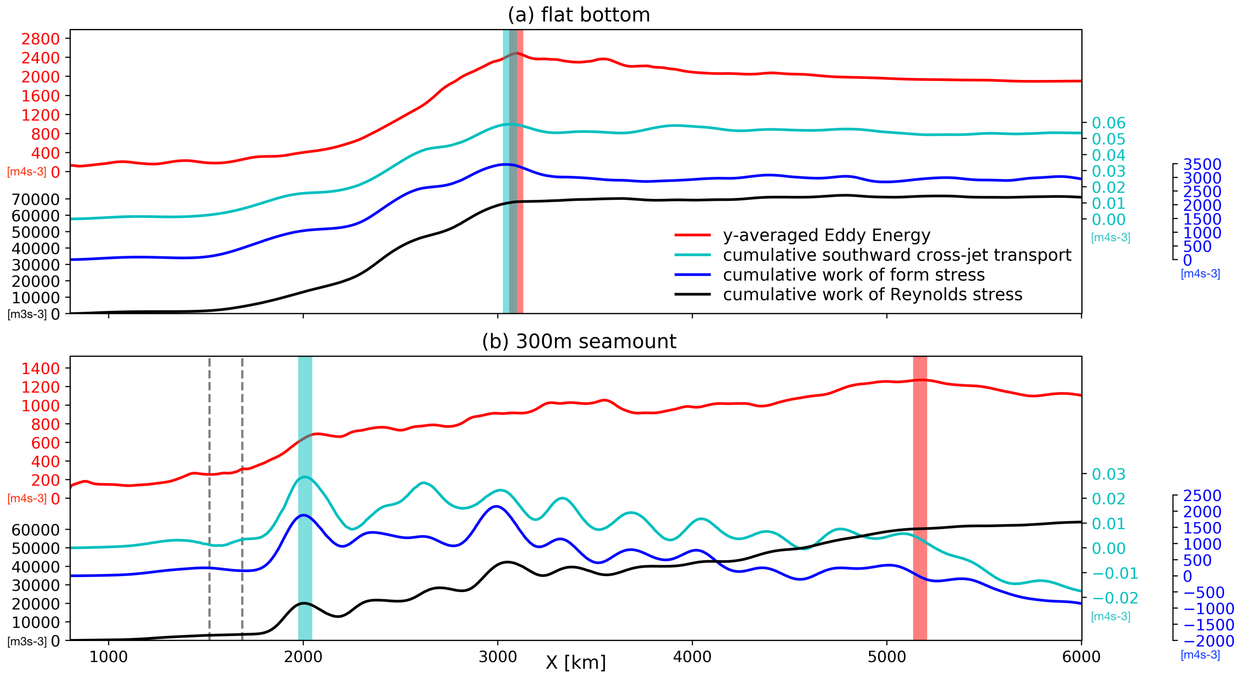

Figure 3. Zonal distributions of energy conversion terms when an unstable jet evolves over (a) a flat bottom, (b) encounters a 300m-tall seamount. The total eddy energy averaged over the channel (red), the along-jet cumulative eddy-driven southward transport across the time-mean jet ('eddy upwelling') (light blue), the along-jet cumulative work of interfacial form stress due to baroclinic instability (dark blue) and cumulative work by Reynolds stress due to barotropic instability (black) are shown. The latter energy conversions terms are both calculated for the upper layer, and are positive when energy is fluxed from the mean into the eddy field. The grey dashed lines indicate the half-width of the topography. For each simulation, the location of maximum total eddy energy is marked by the red shading (indicating the transition between regions of along-stream eddy growth and decay), while the cyan shading marks a significant transition between southward and northward cross-jet eddy transport.

zonal patterns, as illustrated by the flat bottom case (Fig. 3a). Nevertheless, it is important to keep in mind that baroclinic instability alone provides the dynamical mechanism to generate cross-jet transport and eddy upwelling. As such, it is possible that along-stream eddy growth can occur in regions without net southward eddy transport (i.e. without active baroclinic instability) when, for instance, horizontal shear instability is responsible for eddy energy growth. This scenario is nicely illustrated by the 300 m seamount case (Fig. 3b).

These examples speak to the method by which topography influences the eddy-induced transport. We infer that the topographic obstacles affect the flow in such a way that either baroclinic or barotropic instability, or both, are enhanced. In some, but not all, cases there is a strong correspondence between these two different instability mechanisms. However, southward eddy-induced transport is only dependent on the action of baroclinic instability, where isopycnal interfaces slump to release available potential energy into the eddy field.

4 Implications for eddy parameterisations

Our results suggest that energy conversion terms are an unambiguous indicator of eddy-induced cross-jet transport, however, we recognize that these are unlikely to be practical indicators of eddy upwelling in coarse resolution models. Our analysis also indicates that the along-stream growth/decay of eddy energy may be a valuable predictor of eddy upwelling in many cases, and hence may inspire new eddy parameterisations for coarsely-resolved models. Thus, in this section, we assess whether a coarsely-resolved zonal pattern of eddy energy may be used to estimate the cross-jet transport occurring in that region. For that purpose, we compare transport estimates obtained from assuming transport is proportional to the rate of along-stream eddy energy growth to those employing other common parameterizations for eddy upwelling based on large-scale variables, such as the mean isopycnal slope, EKE and EPE. Specifically we consider parameterizations based on the following relationships:

(a) Transport can be parameterised as a constant diffusivity applied to the time-mean isopycnal slope ($\bar{S}$): $X_{jt}^{GM}(x) = \kappa\bar{S} + B$, with a constant $\kappa = A$, inspired by Gent & McWilliams (1990);

(b) The diffusivity κ is proportional to EKE: $X_{jt}^{J}(x) = A.EKE \cdot \bar{S} + B$, inspired by Jansen et al. (2015);

(c) Eddy transport is proportional to the barotropic EPE: $X_{jt}^{EPE}(x) = A.EPEbt + B$, with $EPEbt = \frac{\rho_0}{2} g\overline{\eta'^2}$ (ρ_0: reference density; g: gravitational acceleration; η: sea surface height), inspired by Foppert et al. (2017);

(d) Eddy transport is proportional to the rate of along-stream eddy energy growth: $X_{jt}^{dxEE}(x) = A.\frac{d}{dx}EE + B$ where EE denotes total eddy energy.

(e) Eddy transport is proportional to the local eddy form stress (EFS): $X_{jt}^{EFS}(x) = A.EFS + B$, used as a reference in this exercise.

To compare the relative performance of these parameterisations in our model configuration, the large-scale variable on which each parameterisation is based ($\bar{S}$, EKE, EPEbt, EE or EFS) was smoothed and sub-sampled to a 80km horizontal resolution, roughly equivalent to output from a 1° ocean model. In each case, a least-squares fit was performed to determine the parameters A and B that minimise the total error in transport over the domain. The parameterised transport is then compared to the modeled transport in four different cases (Fig. 4). We place a caveat on the results that follow, which is that the list of eddy parameterisations evaluated is by no means exhaustive. In addition, the comparison presented here allow the parameters to be fitted for each case, while a more systematic parameterisation may require the parameter values to work uniformly across cases.

Results from this exercise confirm the conclusions from the previous section. Local values of energy reservoirs, such as EPE, are not a good indicator of cross-jet transport (e.g. Fig. 4.A3 for the flat-bottom case). The zonal variations in EPE and transport are so different that minimising the total error leads to applying a small southward transport almost uniformly over the whole domain, leading to compensating over-estimated transport upstream (light gray) and under-estimated transport further downstream (dark gray). Similarly, the other relationships based on time-mean isopycnal slope and EKE (Fig. 4A.1-2) fail to capture the zonal pattern of transport, with the best parameterisation being an almost uniform transport of small magnitude.

In contrast, the zonal growth rate of total eddy energy, $\frac{d}{dx}EE$, is able to reproduce the zonal variations in eddy transport, producing a parameterised transport which adequately portrays regions of little to no transport, and regions of localised, enhanced transport. Local eddy form stress is overall the best indicator for eddy transport, but is unlikely to be readily available output from climate models or observations. In the absence of eddy form stress, the zonal growth of eddy energy may be a valuable indicator of where eddy-induced transport occurs, and outperforms commonly used parameterisations of eddy upwelling, in most cases considered in this study (see Supporting Information). One exception is the 300m seamount case (Fig. 4.C1-4) where the relationship between cross-jet transport and the along-stream rate of change of total eddy energy breaks down (Fig. 3b) due to the influence of barotropic instability in generating eddy energy.

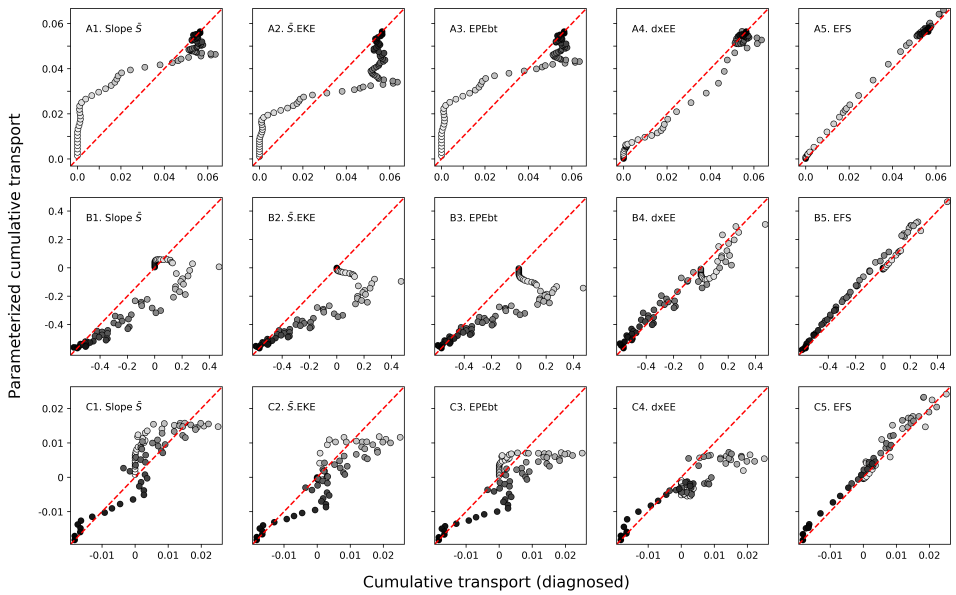

Figure 4. Parameterised cumulative southward transport across the jet axis plotted against the resolved cumulative transport, at each zonal gridpoint along the time-mean jet axis, for A. flat bottom, B. 150m ridge, and C. 300m seamount. Data points are colored from light to dark as we move downstream. In each case, the parameterisation is the best linear fit (by least-square method) that minimises the total error between local values of transport and local 1) time-mean cross-jet isopycnal slope $\bar{S}$, 2) EKE times $\bar{S}$, 3) barotropic EPE ($EPEbt$), 4) zonal growth of total eddy energy (dxEE), and 5) eddy form stress (EFS), where each variable was smoothed and sub-sampled to a 80km resolution.

5 Discussion

This study highlights that eddy-driven cross-jet transport within a shoaling isopycnal occurs in regions of eddy energy growth through baroclinic instability. The presence of topography leads to enhanced eddy upwelling in the region immediately downstream of the obstacle (especially in the first meander) because it modifies the growth of baroclinic instability. The idealised set-up allows exact calculations of quantities not usually diagnosed in global climate models, and the simulations performed in this study provide a plausible mechanism explaining the location of the upwelling pathways from Tamsitt et al. (2017) which occurs in regions upstream of EKE maxima, and further the offset between the divergent eddy heat flux and EKE discussed by Foppert et al. (2017). Simple parameterisations based on mean isopycnal slope, EKE and EPE fail to reproduce this strong, localised, eddy transport near topography. In most cases, the along-stream growth of eddy energy is a good indicator for southward transport, with the exception of cases where barotropic instability and baroclinic instability have distinct growth regions (e.g. a steep isolated seamount; Fig. 4C4).

The benefit of an idealized set-up is that it allows exact calculations of both the eddy form stress and the Reynolds stress, and we can thereby attribute dynamical relevance between the two without ambiguity (noting that these quantities are not usually diagnosed from global climate models or observations). However, the simplified vertical structure in this two-layer system leads to an exaggerated impact of topography, as small values of topography are more dynamically relevant to the ACC. Idealised simulations may also over-stimulate barotropic instability near topography (e.g., Barthel et al., 2017; Youngs et al., 2017). Despite this caveat, we argue that the two-layer set up provides useful dynamical insight, given that evidence of mixed barotropic-baroclinic instability is also observed in the Drake Passage (Foppert, 2019) and may be important for the momentum balance in the ACC (Constantinou & Hogg, 2019).

In this study, we focused only on eddy-induced isopycnal thickness fluxes and showed that eddy-driven upwelling does not occur in regions of high eddy energy, but rather in regions of along-stream eddy energy growth by baroclinic instability. However, the presence of high eddy energy, and potentially high EKE in particular, may contribute to enhancing other types of transport, such as the upwelling of tracers through increased isopycnal stirring (Abernathey & Ferreira, 2015; Dufour et al., 2015). In addition, the net meridional transport in the Southern Ocean is forced by a combination of factors, including wind stress, surface buoyancy fluxes and diabatic processes in the surface mixed layer; these factors are dominant where layers outcrop at the surface and emphasise the role of the vertical structure of eddy processes in the ACC that are omitted from this study. Results from the adiabatic simulations considered in this study best inform on interior upwelling processes, away from frictional boundaries such as the surface and bottom Ekman layers, and away from locations where diabatic mixing dominates (e.g. close to rough topography).

Keeping in mind the above caveats, the detailed dynamical analysis of these idealised simulations provides an important insight: assuming that high values of EKE and/or EPE indicate regions of strong eddy-driven transport is a misconception. In the Southern Ocean there is increasing evidence of mixed instability near topography, where both barotropic and baroclinic instability mechanisms contribute to the dynamics (Youngs et al., 2017; Barthel et al., 2017; Foppert, 2019). The distinct role of each instability mechanism, and their interaction, need to be considered when developing eddy transport parameterisations that will respond physically to changes in ocean dynamics.

6 Open Research

The simulation data and scripts used in the study are freely available on the Zenodo repository at DOI: 10.5281/zenodo.2542957.

Acknowledgments

AB was partially supported by the RGCM program of the US Department of Energy. SW acknowledges support from the Australian Research Council (DE120102927) and the National Science and Engineering Research Council of Canada (22R23085). SRK was supported by a UNSW Silverstar research grant. This research was undertaken on the NCI National Facility in Canberra, Australia, supported by the Australian Commonwealth Government.

References

Abernathey, R., & Cessi, P. (2014). Topographic Enhancement of Eddy Efficiency in Baroclinic Equilibration. *Journal of Physical Oceanography*, *44*(8), 2107–2126. doi: 10.1175/JPO-D-14-0014.1

Abernathey, R., & Ferreira, D. (2015). Southern Ocean isopycnal mixing and ventilation changes driven by winds. *Geophysical Research Letters*, *42*, 10357–10365. doi: 10.1002/2015GL066238

Adcroft, A., Anderson, W., Balaji, V., Blanton, C., Bushuk, M., Dufour, C. O., ... Zhang, R. (2019). The GFDL Global Ocean and Sea Ice Model OM4.0: Model Description and Simulation Features. *J. Adv. Model. Earth Syst.*, 3167–3211. doi: 10.1029/2019MS001726

Aiki, H., & Richards, K. J. (2008). Energetics of the Global Ocean: The Role of Layer-Thickness Form Drag. *Journal of Physical Oceanography*, *38*(9), 1845–1869. doi: 10.1175/2008JPO3820.1

Armour, K. C., Marshall, J., Scott, J. R., Donohoe, A., & Newsom, E. R. (2016).

Southern Ocean warming delayed by circumpolar upwelling and equatorward transport. *Nature Geoscience*, *9*(7), 549–554. doi: 10.1038/ngeo2731

Barthel, A., McC. Hogg, A., Waterman, S., & Keating, S. (2017). Jet–Topography Interactions Affect Energy Pathways to the Deep Southern Ocean. *Journal of Physical Oceanography*, *47*(7), 1799–1816. doi: 10.1175/JPO-D-16-0220.1

Bischoff, T., & Thompson, A. F. (2014). Configuration of a Southern Ocean Storm Track. *Journal of Physical Oceanography*, *44*, 3072–3078. doi: 10.1175/JPO-D-14-0062.1

Chapman, C. C., Hogg, A. M., Kiss, A. E., & Rintoul, S. R. (2015). The Dynamics of Southern Ocean Storm Tracks. *Journal of Physical Oceanography*, *45*, 884–903. doi: 10.1175/JPO-D-14-0075.1

Constantinou, N. C., & Hogg, A. M. (2019). Eddy saturation of the southern ocean: A baroclinic versus barotropic perspective. *Geophysical Research Letters*, *46*(21), 12202-12212. Retrieved from `https://agupubs.onlinelibrary.wiley.com/doi/abs/10.1029/2019GL084117` doi: 10.1029/2019GL084117

Dufour, C. O., Griffies, S. M., de Souza, G. F., Frenger, I., Morrison, A. K., Palter, J. B., ... Slater, R. D. (2015). Role of Mesoscale Eddies in Cross-Frontal Transport of Heat and Biogeochemical Tracers in the Southern Ocean. *Journal of Physical Oceanography*, *45*(12), 3057–3081. Retrieved from `http://journals.ametsoc.org/doi/10.1175/JPO-D-14-0240.1` doi: 10.1175/JPO-D-14-0240.1

Dufour, C. O., Sommer, L. L., Zika, J. D., Gehlen, M., Orr, J. C., Mathiot, P., & Barnier, B. (2012). Standing and transient eddies in the response of the Southern Ocean meridional overturning to the Southern annular mode. *Journal of Climate*, *25*, 6958–6974. doi: 10.1175/JCLI-D-11-00309.1

Foppert, A. (2019). Observed storm track dynamics in drake passage. *Journal of Physical Oceanography*, *49*(3), 867-884. doi: 10.1175/JPO-D-18-0150.1

Foppert, A., Donohue, K. A., Watts, D. R., & Tracey, K. L. (2017). Eddy heat flux across the antarctic circumpolar current estimated from sea surface height standard deviation. *Journal of Geophysical Research: Oceans*, *122*(8), 6947-6964. doi: 10.1002/2017JC012837

Frenger, I., Münnich, M., Gruber, N., & Knutti, R. (2015). Southern Ocean eddy phenomenology. *Journal of Geophysical Research: Oceans*, *120*, 7413–7449. doi:

10.1002/2015JC011047

Fu, L.-L., Chelton, D., Le Traon, P.-Y., & Morrow, R. (2010). Eddy Dynamics From Satellite Altimetry. *Oceanography*, *23*(4), 14–25. doi: 10.5670/oceanog.2010.02

Gent, P. R., & McWilliams, J. C. (1990). *Isopycnal Mixing in Ocean Circulation Models* (Vol. 20) (No. 1). doi: 10.1175/1520-0485(1990)020⟨0150:IMIOCM⟩2.0.CO;2

Hallberg, R., & Gnanadesikan, A. (2001). An Exploration of the Role of Transient Eddies in Determining the Transport of a Zonally Reentrant Current. *Journal of Physical Oceanography*, *31*, 3312–3330.

Hogg, A. M., Meredith, M. P., Chambers, D. P., Abrahamsen, E. P., Hughes, C. W., & Morrison, A. K. (2015). Recent trends in the Southern Ocean eddy field. *Journal of Geophysical Research C: Oceans*, *120*, 257–267. doi: 10.1002/2014JC010470

Holloway, G. (1986). Estimation of oceanic eddy transports from satellite altimetry. *Nature*, *323*, 243-244.

Hughes, C. W., & Ash, E. R. (2001). Eddy forcing of the mean flow in the Southern Ocean. *Journal of Geophysical Research*, *106*(C2), 2713. doi: 10.1029/2000JC900332

Jansen, M. F., Adcroft, A. J., Hallberg, R., & Held, I. M. (2015). Parameterization of eddy fluxes based on a mesoscale energy budget. *Ocean Modelling*, *92*, 28–41. doi: 10.1016/j.ocemod.2015.05.007

Le Quéré, C., Rödenbeck, C., Buitenhuis, E. T., Conway, T. J., Langenfelds, R., Gomez, A., … Heimann, M. (2007). Saturation of the southern ocean CO2 sink due to recent climate change. *Science*, *316*(5832), 1735–1738. doi: 10.1126/science.1136188

Lumpkin, R., & Speer, K. (2007). Global Ocean Meridional Overturning. *Journal of Physical Oceanography*, *37*(10), 2550–2562. doi: 10.1175/JPO3130.1

Marshall, G. J. (2003). Trends in the Southern Annular Mode from Observations and Reanalyses. *Journal of Climate*, *16*(24), 4134–4143. doi: 10.1175/1520-0442(2003)016⟨4134:TITSAM⟩2.0.CO;2

Marshall, J., & Speer, K. (2012, feb). Closure of the meridional overturning circulation through Southern Ocean upwelling. *Nature Geoscience*, *5*(3), 171–180. Retrieved from `http://www.nature.com/doifinder/10.1038/ngeo1391` doi:

10.1038/ngeo1391

Meredith, M. P., & Hogg, A. M. (2006). Circumpolar response of Southern Ocean eddy activity to a change in the Southern Annular Mode. *Geophysical Research Letters*, *33*(16), 2–5. doi: 10.1029/2006GL026499

Olbers, D., Borowski, D., Völker, C., & Wolff, J. O. (2004). The dynamical balance, transport and circulation of the antarctic circumpolar current. *Antarctic science*, *16*(4), 439–470. Retrieved from `http://dx.doi.org/10.1017/S0954102004002251` doi: 10.1017/S0954102004002251

Patara, L., Böning, C. W., & Biastoch, A. (2016). Variability and trends in Southern Ocean eddy activity in 1/12° ocean model simulations. *Geophysical Research Letters*, *43*(9), 4517–4523. doi: 10.1002/2016GL069026

Prandtl, L. (1925). Bericht ber untersuchungen zur ausgebildeten turbulenz. *Z. Angew. Math. Mech.*, *5*, 136.

Sheen, K. L., Naveira Garabato, A. C., Brearley, J. A., Meredith, M. P., Polzin, K. L., Smeed, D. A., . . . Watson, A. J. (2014). Eddy-induced variability in Southern Ocean abyssal mixing on climatic timescales. *Nature Geoscience*, *7*(8), 577–582. doi: 10.1038/ngeo2200

Sokolov, S., & Rintoul, S. R. (2009). Circumpolar structure and distribution of the Antarctic Circumpolar Current fronts: 1. Mean circumpolar paths. *Journal of Geophysical Research: Oceans*, *114*, C11018. doi: 10.1029/2008JC005108

Tamsitt, V., Drake, H. F., Morrison, A. K., Talley, L. D., Dufour, C. O., Gray, A. R., . . . Weijer, W. (2017). Spiraling pathways of global deep waters to the surface of the Southern Ocean. *Nature Communications*, *8*(1), 1–10. doi: 10.1038/s41467-017-00197-0

Thompson, A. F. (2010). Jet Formation and Evolution in Baroclinic Turbulence with Simple Topography. *Journal of Physical Oceanography*, *40*(2), 257–278. doi: 10.1175/2009JPO4218.1

Thompson, A. F., & Naveira Garabato, A. C. (2014). Equilibration of the Antarctic Circumpolar Current by Standing Meanders. *Journal of Physical Oceanography*, *44*(7), 1811–1828. doi: 10.1175/JPO-D-13-0163.1

Thompson, A. F., & Sallée, J. (2012). Jets and Topography: Jet Transitions and the Impact on Transport in the Antarctic Circumpolar Current. *Journal of Physical Oceanography*, *42*(6), 956–972. doi: 10.1175/JPO-D-11-0135.1

Viglione, G. a., & Thompson, A. F. (2016). Lagrangian pathways of upwelling in the Southern Ocean. *Journal of Geophysical Research: Oceans*, *121*(8), 6295–6309. doi: 10.1002/2016JC011773

Waterman, S., Naveira Garabato, A. C., & Polzin, K. L. (2013). Internal Waves and Turbulence in the Antarctic Circumpolar Current. *Journal of Physical Oceanography*, *43*(2), 259–282. doi: 10.1175/JPO-D-11-0194.1

Watts, D. R., Tracey, K. L., Donohue, K. A., & Chereskin, T. K. (2016). Estimates of eddy heat flux crossing the antarctic circumpolar current from observations in drake passage. *Journal of Physical Oceanography*, *46*(7), 2103-2122. doi: 10.1175/JPO-D-16-0029.1

Youngs, M. K., Thompson, A. F., Lazar, A., & Richards, K. J. (2017). ACC Meanders, Energy Transfer, and Mixed Barotropic–Baroclinic Instability. *Journal of Physical Oceanography*, *47*(6), 1291–1305. doi: 10.1175/JPO-D-16-0160.1

Zika, J. D., Le Sommer, J., Dufour, C. O., Molines, J.-M., Barnier, B., Brasseur, P., … Vivier, F. (2013). Vertical Eddy Fluxes in the Southern Ocean. *Journal of Physical Oceanography*, *43*(5), 941–955. doi: 10.1175/JPO-D-12-0178.1

Supporting Information for "Baroclinic control of Southern Ocean eddy upwelling near topography"

Alice Barthel[1], Andrew M. Hogg[2], Stephanie Waterman[3], Shane Keating[4]

[1]Los Alamos National Laboratory, Los Alamos, NM, USA.

[2]Research School of Earth Sciences, Australian National University, Canberra, ACT, Australia.

[3]Department of Earth, Ocean and Atmospheric Sciences, University of British Columbia, Vancouver, BC, Canada.

[4]University of New South Wales, Sydney, NSW, Australia.

Contents of this file

This supporting information provides details of the energy equations in a two-layer isopycnal framework.

Energy budget in a two-layer isopycnal framework

1. Definitions and decompositons

In this study, we use a thickness-weighted energy framework similar to that used by Barthel et al. (2017). The two-layer system has four main energy reservoirs, defined as follows. APE_{bt} is the available potential energy due to the free surface elevation η_0 (or 'barotropic' potential energy)

$$APE_{bt} = \frac{\rho_0}{2} g {\eta_0}^2, \tag{1}$$

APE_{bc} is the available potential energy due to the motions of the interface separating the upper and lower layers η_1 (or 'baroclinic' potential energy)

$$APE_{bc} = \frac{\rho_0}{2} g' {\eta_1}^2, \tag{2}$$

and KE_i is the kinetic energy in each layer ($i = 1, 2$),

$$KE_i = \frac{\rho_0}{2} h_i |\mathbf{u}_i|^2, \quad \text{(for } i = 1, 2\text{)}. \tag{3}$$

Here, ρ_0 is the reference density of the Boussinesq approximation, g is the acceleration due to gravity, $g' = \frac{g\Delta\rho}{\rho_0}$ is the reduced gravity of the interface between the two layers, h_i is the i-th layer thickness, and $\mathbf{u}_i = [u_i, v_i]$ is the horizontal velocity in layer i.

To separate the mean and eddy terms, we define the traditional Reynolds decomposition for most variables in our model. For example, the layer thickness becomes:

$$h_i \equiv \overline{h_i} + h_i', \tag{4}$$

where the overbar and prime symbols denote a three-year time mean and the associated deviation respectively. Following the methodology used in Aiki & Richards (2008), the velocity variable is decomposed into a thickness-weighted mean (TWM) velocity $\widehat{\mathbf{u}}$ and deviation from the TWM mean $\mathbf{u}_i''$,

$$\mathbf{u}_i \equiv \widehat{\mathbf{u}}_i + \mathbf{u}_i'', \text{ with } \widehat{\mathbf{u}}_i \equiv \frac{\overline{h_i \mathbf{u}_i}}{\overline{h_i}}. \tag{5}$$

In a thickness-weighted framework, each energy reservoir can be decomposed into contributions from the mean and eddy, as proposed by **?**,

$$\overline{APE_{bt}} = \overline{\frac{\rho_0}{2} g {\eta_0}^2} = \underbrace{\frac{\rho_0}{2} g \overline{\eta_0}^2}_{MPE_{bt}} + \underbrace{\frac{\rho_0}{2} g \overline{{\eta_0}'^2}}_{EPE_{bt}}, \tag{6}$$

$$\overline{APE_{bc}} = \overline{\frac{\rho_0}{2} g' (\eta_1)^2} = \underbrace{\frac{\rho_0}{2} g' (\overline{\eta_1})^2}_{MPE_{bc}} + \underbrace{\frac{\rho_0}{2} g' \overline{\eta_1'^2}}_{EPE_{bc}}, \tag{7}$$

$$\overline{KE_i} = \overline{\frac{\rho_0}{2} h_i |\mathbf{u}_i|^2} = \underbrace{\frac{\rho_0}{2} \overline{h_i} |\widehat{\mathbf{u}}_i|^2}_{MKE_i} + \underbrace{\frac{\rho_0}{2} \overline{h_i |\mathbf{u}_i''^2}}_{EKE_i}, \quad (\text{for } i = 1, 2). \tag{8}$$

Note that the kinetic energy is decomposed using the TWM decomposition of velocity. Note also that this eddy-mean decomposition is based on the separation between stationary (i.e. mean) and transient (i.e. eddy) features. Thus, the contribution of stationary meanders, or stationary eddies, are included in the contribution of the time-mean flow.

2. Time evolution of the mean and eddy energy

The equations governing the two-layer system can be derived from the incompressible hydrostatic equations of motion in isopycnal coordinates (see Barthel et al. (2017) for the full derivation). In particular, the time-mean energy reservoirs are governed by:

$$\partial_t MPE_{bt} = (\overline{h_1}\widehat{\mathbf{u}}_1 + \overline{h_2}\widehat{\mathbf{u}}_2) \cdot \nabla \overline{\phi_1} - \nabla \cdot (\overline{\phi_1}(\overline{h_1}\widehat{\mathbf{u}}_1 + \overline{h_2}\widehat{\mathbf{u}}_2)) \ , \tag{9}$$

$$\partial_t MPE_{bc} = \overline{h_2}\widehat{\mathbf{u}}_2 \cdot \nabla(\overline{\phi_2} - \overline{\phi_1}) - \nabla \cdot ((\overline{\phi_2} - \overline{\phi_1})\overline{h_2}\widehat{\mathbf{u}}_2)) \ , \tag{10}$$

$$\begin{aligned} \partial_t MKE_i = & -\nabla \cdot (\widehat{\mathbf{u}}_i MKE_i) - \overline{h_i}\widehat{\mathbf{u}}_i \cdot \nabla \overline{\phi_i} - \widehat{\mathbf{u}}_i \cdot \overline{h_i' \nabla \phi_i'} \\ & -\rho_0 (\widehat{\mathbf{u}}_i \cdot \nabla) \cdot \overline{(h_i \mathbf{u}_i'' \mathbf{u}_i'')} + \rho_0 \overline{h_i \mathbf{F}_{\tau \mathbf{i}}} \cdot \widehat{\mathbf{u}}_i, \quad (\text{for } i = 1, 2). \end{aligned} \tag{11}$$

The equation governing the mean component of the layer MP flux divergence is

$$\nabla \cdot (\overline{\phi_i}\, \overline{h_i}\widehat{\mathbf{u}}_i) = -\overline{\phi_i}\, \overline{\partial_t h_i} + \overline{h_i}\widehat{\mathbf{u}}_i \cdot \nabla \overline{\phi_i}, \quad (\text{for } i = 1, 2). \tag{12}$$

Likewise, the eddy energy reservoirs are governed by the following equations:

$$\partial_t EPE_{bt} = \overline{\phi_1' \partial_t h_2'} + \overline{\phi_1' \partial_t h_1'} \tag{13}$$

$$\partial_t EPE_{bc} = \overline{\phi_2' \partial_t h_2'} - \overline{\phi_1' \partial_t h_2'} \tag{14}$$

$$\begin{aligned} \partial_t EKE_i = & -\nabla \cdot (\widehat{\mathbf{u}}_i \ EKE_i) - \nabla \cdot (\overline{\mathbf{u}_i'' EKE_i}) - \overline{\mathbf{u}_i'' \cdot h_i \nabla \phi_i'} \\ & + \rho_0 \widehat{\mathbf{u}}_i \cdot \nabla \cdot \overline{(h_i \mathbf{u}_i'' \otimes \mathbf{u}_i'')} + \rho_0 \overline{h_i \boldsymbol{F_{\tau i}} \cdot \mathbf{u}_i''}, \quad (\text{for } i = 1, 2), \end{aligned} \tag{15}$$

where $\otimes$ denotes the outer product of two vectors. The associated eddy MP flux divergence equation is:

$$\nabla \cdot (\overline{\phi_i' h_i'} \widehat{\mathbf{u}}_i + \overline{\phi_i' h_i \mathbf{u}_i''}) = -\overline{\phi_i' \partial_t h_i'} + \widehat{\mathbf{u}}_i \cdot \overline{h_i' \nabla \phi_i'} + \overline{h_i \mathbf{u}_i'' \nabla \phi_i'} \tag{16}$$

These equations include advective terms, expressed as flux divergences, and local conversion terms. Only two terms locally convert energy between the time-mean and the eddy components of the system in layer i:

1. the work of interfacial form stress, $-\widehat{\mathbf{u}}_i \cdot \overline{h_i' \nabla \phi_i'}$, responsible for the generation of eddy energy in baroclinic instability, and
2. the work of Reynolds stress due to the horizontal convergence of momentum, $\rho_0 \widehat{\mathbf{u}}_i \cdot \nabla \cdot \overline{(h_i \mathbf{u}_i'' \otimes \mathbf{u}_i'')}$, which is associated with barotropic instability.

These terms can be bi-directional but are here defined as positive when converting energy from the mean to the eddy field.

References

Abernathey, R., & Cessi, P. (2014). Topographic Enhancement of Eddy Efficiency in Baroclinic Equilibration. *Journal of Physical Oceanography*, *44*(8), 2107–2126. doi:

10.1175/JPO-D-14-0014.1

Abernathey, R., & Ferreira, D. (2015). Southern Ocean isopycnal mixing and ventilation changes driven by winds. *Geophysical Research Letters*, *42*, 10357–10365. doi: 10.1002/2015GL066238

Adcroft, A., Anderson, W., Balaji, V., Blanton, C., Bushuk, M., Dufour, C. O., ... Zhang, R. (2019). The GFDL Global Ocean and Sea Ice Model OM4.0: Model Description and Simulation Features. *J. Adv. Model. Earth Syst.*, 3167–3211. doi: 10.1029/2019MS001726

Aiki, H., & Richards, K. J. (2008). Energetics of the Global Ocean: The Role of Layer-Thickness Form Drag. *Journal of Physical Oceanography*, *38*(9), 1845–1869. doi: 10.1175/2008JPO3820.1

Armour, K. C., Marshall, J., Scott, J. R., Donohoe, A., & Newsom, E. R. (2016). Southern Ocean warming delayed by circumpolar upwelling and equatorward transport. *Nature Geoscience*, *9*(7), 549–554. doi: 10.1038/ngeo2731

Barthel, A., McC. Hogg, A., Waterman, S., & Keating, S. (2017). Jet–Topography Interactions Affect Energy Pathways to the Deep Southern Ocean. *Journal of Physical Oceanography*, *47*(7), 1799–1816. doi: 10.1175/JPO-D-16-0220.1

Bischoff, T., & Thompson, A. F. (2014). Configuration of a Southern Ocean Storm Track. *Journal of Physical Oceanography*, *44*, 3072–3078. doi: 10.1175/JPO-D-14-0062.1

Chapman, C. C., Hogg, A. M., Kiss, A. E., & Rintoul, S. R. (2015). The Dynamics of Southern Ocean Storm Tracks. *Journal of Physical Oceanography*, *45*, 884–903. doi: 10.1175/JPO-D-14-0075.1

Constantinou, N. C., & Hogg, A. M. (2019). Eddy saturation of the southern ocean:

A baroclinic versus barotropic perspective. *Geophysical Research Letters*, *46*(21), 12202-12212. Retrieved from https://agupubs.onlinelibrary.wiley.com/doi/abs/10.1029/2019GL084117 doi: 10.1029/2019GL084117

Dufour, C. O., Griffies, S. M., de Souza, G. F., Frenger, I., Morrison, A. K., Palter, J. B., ... Slater, R. D. (2015). Role of Mesoscale Eddies in Cross-Frontal Transport of Heat and Biogeochemical Tracers in the Southern Ocean. *Journal of Physical Oceanography*, *45*(12), 3057–3081. Retrieved from http://journals.ametsoc.org/doi/10.1175/JPO-D-14-0240.1 doi: 10.1175/JPO-D-14-0240.1

Dufour, C. O., Sommer, L. L., Zika, J. D., Gehlen, M., Orr, J. C., Mathiot, P., & Barnier, B. (2012). Standing and transient eddies in the response of the Southern Ocean meridional overturning to the Southern annular mode. *Journal of Climate*, *25*, 6958–6974. doi: 10.1175/JCLI-D-11-00309.1

Foppert, A. (2019). Observed storm track dynamics in drake passage. *Journal of Physical Oceanography*, *49*(3), 867-884. doi: 10.1175/JPO-D-18-0150.1

Foppert, A., Donohue, K. A., Watts, D. R., & Tracey, K. L. (2017). Eddy heat flux across the antarctic circumpolar current estimated from sea surface height standard deviation. *Journal of Geophysical Research: Oceans*, *122*(8), 6947-6964. doi: 10.1002/2017JC012837

Frenger, I., Münnich, M., Gruber, N., & Knutti, R. (2015). Southern Ocean eddy phenomenology. *Journal of Geophysical Research: Oceans*, *120*, 7413–7449. doi: 10.1002/2015JC011047

Fu, L.-L., Chelton, D., Le Traon, P.-Y., & Morrow, R. (2010). Eddy Dynamics From Satellite Altimetry. *Oceanography*, *23*(4), 14–25. doi: 10.5670/oceanog.2010.02

Gent, P. R., & McWilliams, J. C. (1990). *Isopycnal Mixing in Ocean Circulation Models* (Vol. 20) (No. 1). doi: 10.1175/1520-0485(1990)020⟨0150:IMIOCM⟩2.0.CO;2

Hallberg, R., & Gnanadesikan, A. (2001). An Exploration of the Role of Transient Eddies in Determining the Transport of a Zonally Reentrant Current. *Journal of Physical Oceanography*, *31*, 3312–3330.

Hogg, A. M., Meredith, M. P., Chambers, D. P., Abrahamsen, E. P., Hughes, C. W., & Morrison, A. K. (2015). Recent trends in the Southern Ocean eddy field. *Journal of Geophysical Research C: Oceans*, *120*, 257–267. doi: 10.1002/2014JC010470

Holloway, G. (1986). Estimation of oceanic eddy transports from satellite altimetry. *Nature*, *323*, 243-244.

Hughes, C. W., & Ash, E. R. (2001). Eddy forcing of the mean flow in the Southern Ocean. *Journal of Geophysical Research*, *106*(C2), 2713. doi: 10.1029/2000JC900332

Jansen, M. F., Adcroft, A. J., Hallberg, R., & Held, I. M. (2015). Parameterization of eddy fluxes based on a mesoscale energy budget. *Ocean Modelling*, *92*, 28–41. doi: 10.1016/j.ocemod.2015.05.007

Le Quéré, C., Rödenbeck, C., Buitenhuis, E. T., Conway, T. J., Langenfelds, R., Gomez, A., . . . Heimann, M. (2007). Saturation of the southern ocean CO2 sink due to recent climate change. *Science*, *316*(5832), 1735–1738. doi: 10.1126/science.1136188

Lumpkin, R., & Speer, K. (2007). Global Ocean Meridional Overturning. *Journal of Physical Oceanography*, *37*(10), 2550–2562. doi: 10.1175/JPO3130.1

Marshall, G. J. (2003). Trends in the Southern Annular Mode from Observations and Reanalyses. *Journal of Climate*, *16*(24), 4134–4143. doi: 10.1175/1520-0442(2003)016⟨4134:TITSAM⟩2.0.CO;2

Marshall, J., & Speer, K. (2012, feb). Closure of the meridional overturning circulation through Southern Ocean upwelling. *Nature Geoscience*, *5*(3), 171–180. Retrieved from `http://www.nature.com/doifinder/10.1038/ngeo1391` doi: 10.1038/ngeo1391

Meredith, M. P., & Hogg, A. M. (2006). Circumpolar response of Southern Ocean eddy activity to a change in the Southern Annular Mode. *Geophysical Research Letters*, *33*(16), 2–5. doi: 10.1029/2006GL026499

Olbers, D., Borowski, D., Völker, C., & Wolff, J. O. (2004). The dynamical balance, transport and circulation of the antarctic circumpolar current. *Antarctic science*, *16*(4), 439–470. Retrieved from `http://dx.doi.org/10.1017/S0954102004002251` doi: 10.1017/S0954102004002251

Patara, L., Böning, C. W., & Biastoch, A. (2016). Variability and trends in Southern Ocean eddy activity in 1/12° ocean model simulations. *Geophysical Research Letters*, *43*(9), 4517–4523. doi: 10.1002/2016GL069026

Prandtl, L. (1925). Bericht ber untersuchungen zur ausgebildeten turbulenz. *Z. Angew. Math. Mech.*, *5*, 136.

Sheen, K. L., Naveira Garabato, A. C., Brearley, J. A., Meredith, M. P., Polzin, K. L., Smeed, D. A., ... Watson, A. J. (2014). Eddy-induced variability in Southern Ocean abyssal mixing on climatic timescales. *Nature Geoscience*, *7*(8), 577–582. doi: 10.1038/ngeo2200

Sokolov, S., & Rintoul, S. R. (2009). Circumpolar structure and distribution of the Antarctic Circumpolar Current fronts: 1. Mean circumpolar paths. *Journal of Geophysical Research: Oceans*, *114*, C11018. doi: 10.1029/2008JC005108

Tamsitt, V., Drake, H. F., Morrison, A. K., Talley, L. D., Dufour, C. O., Gray, A. R.,

. . . Weijer, W. (2017). Spiraling pathways of global deep waters to the surface of the Southern Ocean. *Nature Communications*, *8*(1), 1–10. doi: 10.1038/s41467-017-00197-0

Thompson, A. F. (2010). Jet Formation and Evolution in Baroclinic Turbulence with Simple Topography. *Journal of Physical Oceanography*, *40*(2), 257–278. doi: 10.1175/2009JPO4218.1

Thompson, A. F., & Naveira Garabato, A. C. (2014). Equilibration of the Antarctic Circumpolar Current by Standing Meanders. *Journal of Physical Oceanography*, *44*(7), 1811–1828. doi: 10.1175/JPO-D-13-0163.1

Thompson, A. F., & Sallée, J. (2012). Jets and Topography: Jet Transitions and the Impact on Transport in the Antarctic Circumpolar Current. *Journal of Physical Oceanography*, *42*(6), 956–972. doi: 10.1175/JPO-D-11-0135.1

Viglione, G. a., & Thompson, A. F. (2016). Lagrangian pathways of upwelling in the Southern Ocean. *Journal of Geophysical Research: Oceans*, *121*(8), 6295–6309. doi: 10.1002/2016JC011773

Waterman, S., Naveira Garabato, A. C., & Polzin, K. L. (2013). Internal Waves and Turbulence in the Antarctic Circumpolar Current. *Journal of Physical Oceanography*, *43*(2), 259–282. doi: 10.1175/JPO-D-11-0194.1

Watts, D. R., Tracey, K. L., Donohue, K. A., & Chereskin, T. K. (2016). Estimates of eddy heat flux crossing the antarctic circumpolar current from observations in drake passage. *Journal of Physical Oceanography*, *46*(7), 2103-2122. doi: 10.1175/JPO-D-16-0029.1

Youngs, M. K., Thompson, A. F., Lazar, A., & Richards, K. J. (2017). ACC Meanders, Energy Transfer, and Mixed Barotropic–Baroclinic Instability. *Journal of Physical Oceanography*, *47*(6), 1291–1305. doi: 10.1175/JPO-D-16-0160.1

Zika, J. D., Le Sommer, J., Dufour, C. O., Molines, J.-M., Barnier, B., Brasseur, P., ... Vivier, F. (2013). Vertical Eddy Fluxes in the Southern Ocean. *Journal of Physical Oceanography*, *43*(5), 941–955. doi: 10.1175/JPO-D-12-0178.1